Scaling laws for the flow of generalized Newtonian suspensions

Maxime Liard,[1,2] Nicos S. Martys,[3] William L. George,[3] Didier Lootens,[2] and Pascal Hébraud[1]

[1)] *IPCMS/CNRS, 23 rue du Loess, 67034 Strasbourg Cedex, France*

[2)] *SIKA Technology A.G., Tuffenwies 16, CH-8048 Zürich, Switzerland*

[3)] *National Institute of Standards and Technology,100 Bureau Drive, Gaithersburg, MD 20899-8615, USA*

It has been observed that flow curves (viscosity vs shear rate) of spherical solid inclusions suspended in a generalized Newtonian fluid medium can be rescaled so as to collapse onto the flow curve of the fluid medium. This result is surprising given the range of values and the spatial heterogeneity of local shear rates and viscosity in such systems. We consider such scaling for the cases of shear thinning, Newtonian and shear thickening fluid media. Results from experiment and computational modeling are presented that examine the microscopic origins of this scaling behavior. Over a wide range of volume fractions (5 % to 50 %) it is shown that the distribution of local shear rates can be collapsed onto a single universal curve. The parameters for rescaling the shear rate distributions can be analytically related to the macroscopic rescaling parameters for the viscosity. As a result of this rescaling capability, one may measure the properties of the fluid medium and predict the macroscopic behavior of the suspension.

PACS numbers: 83.80.Hj, 83.60.Rs

I. INTRODUCTION

Suspensions are ubiquitous in nature and are important for a wide variety of technical applications: paints, pastes, cement based materials, slurries, mud, food products, medicine, and drilling fluids. A suspension can be described as a collection of solid bodies (either deformable or rigid) in a fluid medium. An important property of a suspension is its viscosity. It can be thought of as the medium's resistance to flow for a given applied force. That is, given an applied force *per* area on a volume element containing fluid, the resulting shear rate is inversely proportional to the viscosity. It is well known that the viscosity of suspensions increases with its volume fraction. This increase can be computed exactly when the volume fraction of the suspension tends to zero (Batchelor, 1967), by analytically describing the transport of momentum that occurs through both the solid particle phase and the fluid medium. However, as the volume fraction of the suspension increases, such a description does not allow for direct analytic treatment of the suspension viscosity. In addition, the description of the flow can be further complicated by the self-organization of the particles under flow or the onset of jamming (Liu and Nagel, 2001). Semi-empirical models based on the free volume approach (Cohen and Turnbull, 1959) or on the description of the cooperative motion of particles (Götze, 1991) describe the divergence of the viscosity close to the maximum packing concentration (Cheng *et al.*, 2002). Phenomenological expressions have also been devised that account for flow behavior both at the low volume fraction and near the jamming regimes by design. As a result, they generally predict the correct qualitative behavior of the suspension in a wide range of concentrations (Sundstrom, 1983).

The flow description of a suspension is even more complex when the fluid medium exhibits non-Newtonian behavior (*e.g.* viscoelastic or power-law dependence of viscosity on shear rate). Models based on the hypothesis that the increase of the volume fraction leads to an increase of the viscosity proportional to the volume of suspending medium (Roscoe, 1952) have been extended to weakly viscoelastic matrices (Tanner *et al.*, 2010). Moreover, for viscoelastic continuous media, the suspensions exhibit normal stresses. The first normal stress difference is observed to be positive whereas the second normal stress difference is negative in the semi-dilute regime. The magnitude of both increases with the volume fraction of particles (Mall-Gleissle *et al.*, 2002; Tanner *et al.*, 2013; Dai *et al.*, 2014; Tanner *et al.*,

2013). In this article, we do not consider the normal forces, although they may be non-negligible, in particular for the shear thinning polymeric matrix.

Consider the case where the fluid medium is Newtonian (viscosity is a constant independent of shear rate or external forces), shear thinning (viscosity decreases with shear rate) or shear thickening (viscosity increases with shear rate). For a suspension, different points of the continuous medium experience different shear rates, depending on their position relative to neighboring inclusions. As a consequence, if the fluid medium is shear thinning or shear thickening, the viscosity will vary spatially. This spatial heterogeneity of shear rates or viscosity in suspensions has not been studied.

Remarkably, it has been observed that the flow curves (viscosity *vs* shear rate) of non-Newtonian suspensions follow the same form as the continuous medium (Roscoe, 1952; Kataoka *et al.*, 1978), and further, the flow curve of non-Newtonian suspensions may be rescaled onto the flow curve of the continuous fluid medium for a wide range of volume fractions (Barnes, 2003). Thus, there exists a complex microscopic interparticle flow, with possibly widely different local viscosities and stresses, and yet, on the other hand, one obtains a very simple macroscopic behavior. This has been attributed to the fact that, due to the continuous nature of the stress, it is the same everywhere. As a consequence, when expressed as a function of shear stress, flow curves of different volume fraction non-Newtonian suspensions should superpose by shifting the viscosity only (Barnes, 2003; Highgate and Whorlow, 1970).

In this paper we show that such a simple rescaling is not satisfied : the stress needs to be shifted altogether with the viscosity. This may be attributed to the contribution of the out-of-plane particles' motion to the transport of momentum. We also examine the relationship between the macroscopic flow curves and the local flow properties of a suspension in a non-Newtonian fluid medium to gain insight into the remarkable scaling behavior.

To this end, we first perform experimental measurements to determine the constitutive laws (viscosity *vs* shear rate) of suspensions of silica beads in shear thinning and shear thickening matrices. Then, to gain insight into the local flow behavior, computer simulations, based on a Smoothed Particle Hydrodynamics (SPH) approach are used to model the flow of such suspensions. Both experiments and simulations lead to the conclusion that the flow curve of suspensions of concentration ϕ may indeed be superposed onto the

medium flow curve using two scaling parameters, $\dot{\gamma}_{sc}$ and η_{sc} . The scaling parameters can be fundamentally linked together by examining the microscopic flow behavior.

The paper in organized in the following way. In Sec. II, the experimental and numerical techniques are described. The results related to the macroscopic flow behavior are reported in Sec. III. They are discussed in Sec. IV on the basis of local shear rate distributions obtained from the numerical simulations. Sec. V contains conclusions and comments.

II. EXPERIMENTS AND TECHNIQUES

II.1. Experiments

Two different suspending fluids are prepared. For the shear-thinning matrix, 1.5 % in mass of polyethylene oxide ($M_w = 4.10^6$ g.mol^{-1}, POLYOX, Dow) is dispersed in water and is mixed during 10 hours to ensure the homogeneity of the resulting solution.The viscosity at the Newtonian plateau (at low shear rate) is about 10 Pa.s. The shear-thickening matrix is prepared by mixing industrial corn starch (Maizena, Unilever) at 48 w% with a solution consisting of sucrose (35 w% and water).The minimum viscosity is 0.6 Pa.s. The diameter of the corn starch is of the order of 2 μm to 5 μm, that is 10 to 20 times smaller than the diameter of the silica particles. The corn starch suspension will be considered as homogeneous in the subsequent analysis.

Suspensions with different glass bead sizes are then prepared. P0060-beads (Sigmund Lindner, Germany) of diameter range of 50 μm to 70 μm and 100 μm to 140 μm. The beads density is 2.4 g.mL^{-1}. The beads are spherical and stored in dry form. For the shear-thinning suspensions different quantities of beads are added to obtain volume fractions ranging from 0 % to 50 % and the dispersion was made by hand mixing. For the shear-thickening suspensions, the studied volume fractions range 0 % to 40 % for 100 μm diameter beads and 0 % to 30 % for 50 μm diameter beads. Thickening suspensions are dispersed using sonication. All experiments are performed with an Anton Paar MCR 301 rheometer.

Experiments made with the shear-thinning suspending fluid and also with beads of 50 μm in the shear-thickening medium have been performed using a plate-plate geometry of 25 mm diameter and 1 mm gap. Experiments have been performed with the 35 % volume fraction

shear thinning suspension, with gaps 1.5 mm and 2 mm in order to verify that wall slippage is not observed. The system is pre-sheared at 1 s^{-1}during 10 s. Then, a shear-rate sweeping is applied, with in a logarithmic scale from 0.05 s^{-1} to 100 s^{-1} for the shear-thinning suspensions and from 0.05 s^{-1} to 20 s^{-1} for the shear-thickening suspensions. 5 to 10 points *per* decade are recorded and the total duration of the experiments does not exceed 250 seconds. We have checked that all the measurements are performed in the stationary state and the uncertainty of the measured stress has been obtained by repeating the measurements and is equal to or less than 10 %. Experiments with 100 μm beads in cornstarch solution are performed in a Couette cell of 25 mm diameter and 1 mm gap) following the same protocol. Therefore, we recovered the curve viscosity as a function of the shear-rate for our experiments. The atmosphere is saturated with water vapor and evaporation is not observed during the experiments. Sedimentation is not observed despite the size of the beads and their density, measurements at 1 s^{-1} have been performed for a duration longer than the experiments time (300 s) and the measured viscosity is constant during this time range. No fracture have been observed with shear-thinning suspension, meanwhile it occurred with high concentrated shear-thickening suspensions.

II.2. SPH simulations

The computational model of fluid flow utilized for this work is based on a Smoothed Particle Hydrodynamics approach that is a Lagrangian formulation of the Generalized Navier-Stokes equations. The Lagrangian formulation of the continuity equation and the general Navier Stokes equations are (Landau and Lifshitz, 1987):

$$\frac{\partial \rho}{\partial t} = -\rho \nabla \cdot \mathbf{v}, \tag{1}$$

and

$$\rho \frac{\partial v_i}{\partial t} = -\frac{\partial P}{\partial x_i} + \frac{\partial}{\partial x_k}\left\{\eta\left(\frac{\partial v_i}{\partial x_k} + \frac{\partial v_k}{\partial x_i} - \frac{2}{3}\delta_{ik}\nabla \cdot \mathbf{v}\right)\right\} + \frac{\partial}{\partial x_i}\left(\zeta \nabla \cdot \mathbf{v}\right). \tag{2}$$

Here, ρ, is the fluid density, P is pressure, v is velocity, η and ζ are the shear and bulk viscosities, respectively. The indices ($i, j, k \in [1, 2, 3]$) refer to spatial dimension. In these equations the bulk and shear viscosities cannot be taken outside the gradient operator because they can be spatially dependent. In the limit that the viscosity is a constant, the

above equations reduce to the usual Navier-Stokes equations. Note, here the Lagrangian formulation is preferred because it gives us more flexibility in handling moving boundaries. This approach accounts for a spatially varying viscosity that is, for example, dependent on the local shear rates. While details of the computational model are beyond the scope of this paper, we briefly describe some of its features and refer to Martys *et al.* (2010) and references within. In SPH, local material properties are represented throughout a volume by a discrete set of particles f_p where f is, as a fluid property (*e.g.* density and temperature) and the subscript denotes its location. Then to represent the material property as a function in space, $f(\mathbf{r})$, a weighted sum over neighboring discrete points is carried out and typically represented as

$$f(\mathbf{r}) = \sum_q f_q S(|\mathbf{r_q} - \mathbf{r}|) \tag{3}$$

with

$$S(\mathbf{r_q} - \mathbf{r}) = \frac{W(|\mathbf{r_q} - \mathbf{r}|)}{\sum_p W(|\mathbf{r_p} - \mathbf{r}|)} \tag{4}$$

Here $W(|\mathbf{r_q} - \mathbf{r}|)$ is a weight function (see appendix). Note, the number density of particles, d_p, can be written as

$$d_p = \sum_q W(|\mathbf{r_q} - \mathbf{r_p}|) \tag{5}$$

The fluid density, ρ_p, at point, $\mathbf{r_p}$, is then given by $\rho_p = m d_p$, where, m, is the mass. The time evolution of the fluid is represented by a discretized version of the general Navier-Stokes equations (Monaghan, 2005) that updates the values of ρ_p and the velocity, $\mathbf{v}_p$:

$$\left(\frac{\partial \rho}{\partial t}\right)_p = m \sum_q F(|\mathbf{r}_p - \mathbf{r}_q|)(\mathbf{r}_p - \mathbf{r}_q) \cdot (\mathbf{v}_p - \mathbf{v}_q) \tag{6}$$

and

$$\left(\rho \frac{\partial v_i}{\partial t}\right)_p = -\left(\frac{\partial P}{\partial x_i}\right)_p + A_p^i \tag{7}$$

with

$$A_p^i = 5 \sum_q \frac{F(|\mathbf{r}_p - \mathbf{r}_q|)}{\rho_q} \left[\frac{(\eta_p + \eta_q)(\mathbf{r}_p - \mathbf{r}_q)^i (\mathbf{r}_p - \mathbf{r}_q) \cdot (\mathbf{v}_p - \mathbf{v}_q)}{(\mathbf{r}_p - \mathbf{r}_q)^2}\right]. \tag{8}$$

For this discrete representation of the Navier-Stokes equations we have taken $\zeta = \frac{5}{3}\eta$ and,

$$F(r) = \left(\frac{315}{4\pi}\right)(1-r)^2 . \tag{9}$$

is related to the gradient of $W(r)$ (appendix). This form assumes that $\zeta = \frac{5}{3}\eta$. To account for the pressure gradient term, we follow the previous work of Monaghan (2005) :

$$(\nabla P)_p = -m\rho_p \sum_q \left(\frac{P_p}{\rho_p^2} + \frac{P_q}{\rho_q^2}\right) F(|\mathbf{r}_p - \mathbf{r}_q|)(\mathbf{r}_p - \mathbf{r}_q) \tag{10}$$

A pressure term, commonly used to model incompressible fluids, is given as $P = c^2(\rho - \rho_{eq})$ where c is the speed of sound, ρ_{eq} is an equilibrium density of the SPH particles.

When determining the local value of the viscosity it will be first necessary to evaluate the local shear rate tensor. A representation of the discretized shear rate is given by:

$$(\dot{\gamma}_{ij})_p = \sum_q \frac{F(|\mathbf{r}_p - \mathbf{r}_q|)}{\rho_q/m}(\mathbf{r}_p - \mathbf{r}_q)_i(\mathbf{v}_p - \mathbf{v}_q)_j. \tag{11}$$

The local magnitude of the the shear rate is then

$$\dot{\gamma}_p = \sqrt{\frac{\sum_{ij}(\dot{\gamma}_{ij})_p^2}{2}}. \tag{12}$$

This form of discretization is convenient in that its numerical solution lends itself to molecular dynamics techniques where the SPH particles undergo motion in response to effective "interparticle" forces.

To model spherical solid inclusions, we follow the approach used for Dissipative Particle Dynamics (DPD) based simulations by Hoogerbrugge and Koelman (1992) and Martys (2005). Here, the solid inclusion is defined as an assembly of constrained SPH particles so that they form a rigid body. The rigid body motion is then determined by summing the forces due the neighboring SPH particles and having them move according to the Euler equations (Martys and Mountain, 1999).

As described previously (Boek *et al.*, 1997; Martys, 2005), when modeling a dense suspension of hard spheres using this DPD based approach, or, in this case SPH, the particle interactions are not sufficiently strong enough to prevent overlaps of the spheres. Computationally determining realistic flows between neighboring spheres in very close proximity would require a very fine resolution, or a number density of fluid particles that is too high to

make simulations tractable over reasonable times. To avoid this problem, lubrication forces (Kim and Karrila, 1991; Martys, 2005) are explicitly included in the simulation to account for hydrodynamic interactions between neighboring spheres. There are several forms or "modes" of lubrication force interactions between hard spheres. The most well known and important is called the squeeze mode, that accounts for forces that develop as two spheres directly approach each other. This force is proportional to the velocity difference between the spheres and is inversely proportional to the nearest surface-to-surface distance. For the case of monosize spheres, the lubrication force, $\mathbf{F}_{lub}$, is equal to $\frac{3}{2}\pi\eta a_r^2(\mathbf{V}_A - \mathbf{V}_B)/s_{AB}$, where a_r is the sphere radius, $\mathbf{V}_A$ and $\mathbf{V}_B$ are the velocities of spheres "A" and "B", and s_{AB} is the nearest surface to surface distance between spheres labeled A and B. There are additional logarithmic contributions to the squeeze mode as well as other modes like the twist mode, which, as it sounds, describes the effect of one sphere rotating relative to a neighboring sphere. These additional contributions all scale logarithmically with s_{AB} or $s_{AB}\ \ln(s_{AB})$ and are included in the simulations. In addition, the lubrication forces take to account the viscosity dependence of the local shear rate between neighboring sphere surfaces (Martys *et al.*, 2010). A velocity Verlet algorithm as described in Martys and Mountain (1999) was implemented for the numerical time integration of the SPH equations (Martys and Mountain, 1999). To insure stability and accuracy of solution we normally ran simulations with a typical time step, δt, such that $10^{-5} \approx \delta t\dot{\gamma}$. As volume fraction increased the time step needed to be further reduced to prevent overlap of spheres as they came in close proximity with each other. Here a variable time step is also included in our algorithm such that the distance between sphere surfaces was never reduced by more than 10 % over an interval of δt. In our simulations approximately 500 to 1200 spheres were used to represent suspensions with volume fraction ranging from 20 % to 50 % respectively. To model shear flow we used a Lees-Edwards boundary condition (Allen and Tildesley, 1987) which produces a Couette geometry type flow. The simulation approach used in this paper has been demonstrated to recover simple analytic solutions of flow fields of pipe flow for generalized Newtonian fluids and agrees well with experimental data of relative viscosities of suspensions having a Newtonian and generalized Newtonian fluid medium (Martys *et al.*, 2010). A comparison with simulation data obtained by Sierou and Brady (2002) using an alternative but highly accurate method for modeling suspensions with a Newtonian matrix is given in Fig. 2 *insert*. The relative difference between the viscosities is smaller than 0.6 %.

For this paper, a model viscosity, that is shear rate dependent, is used in the simulations that has the form $\eta(\dot{\gamma}) \propto (1 + \frac{\dot{\gamma}}{\dot{\gamma}^*})^{n-1}$ where we take $n = 0.5$ to model a shear thinning fluid and $n = 1.5$ for the shear thickening fluid and $\dot{\gamma}$ is in units of s^{-1}. Note that for $\dot{\gamma} \ll 1\ s^{-1}$ the fluid behaves as if Newtonian. This simple model for the fluid medium viscosity describes well the experimental for the shear thinning matrix (Fig. 1). The shear thinning behavior at low shear rates of the corn starch suspension is not rendered by this phenomenological law, but the high shear rate shear thickening behavior is correctly modeled. We will thus consider in more detail the flow behavior at high shear rates and, when computing the contribution of local stresses to the macroscopic stress, we will consider results obtained at shear rates $\dot{\gamma} = 2\dot{\gamma}^*$, where a good agreement is found between the experiments and the simulations, both for the shear thinning and the shear thickening suspending media. This corresponds to the experimental shear rates equal to 10 s^{-1} for the shear thinning fluid and 3 s^{-1} for the shear thickening continuous matrix.

III. MACROSCOPIC FLOW CURVES

This section compares flow curves from SPH-based simulations with experiments. The results are plotted in Fig. 1 for both shear thinning **(a), (c)** and shear thickening respectively **(b), (d)**. We performed rheological experiments for the shear thinning suspensions of 100 μm diameter particles at volume fractions of 0 %, 5.5 %, 12 %, 18 %, 22 %, 26 %, 29 %, 34 %, 40 %, 45 % and 50 % and associated SPH-simulations at volume fractions of 0 %, 20 %, 30 %, 40 % and 50 %. For the shear thickening suspensions, volume fractions used for experiments and simulations are respectively 0 %, 5 %, 10 %, 20 %, 30 % and 40 % and 0 %, 20 %, 30 % and 40 %. The constitutive laws for the fluid medium used in the SPH simulations, discussed in the previous section, are also plotted in Fig. 1 **(a)** and **b)**. Results for 50 μm diameter particles are given in Fig 1 **(c)** (volume fractions 0 %, 5 %, 10 %, 20 %, 30 %, 35 %, 40 %, 42.5 %, 45 %, and 47.5 %) shear thinning medium, and **(d)** (volume fractions 0 %, 5 %, 10 %, 15 %, 20 %, 25 %, and 30 %).

For the shear thinning suspensions studied, at any volume fraction, there are two different asymptotic behaviors for viscosity. At low shear rate ($\dot{\gamma} \ll 1\ s^{-1}$) the behavior is approximately Newtonian, while at high shear rate ($\dot{\gamma} \gg 1\ s^{-1}$) the behavior is shear thinning with

a slope independent of the volume fraction, *i.e.* $\eta_\phi(\dot\gamma) \sim \dot\gamma^{n-1}$ where $n \in]0,1[$. Similarly, for the shear thickening suspensions, two different behaviors are present : shear thinning at low shear rate ($\dot\gamma \ll 1\ s^{-1}$) and a shear thickening regime at high-shear rate ($\dot\gamma \gg 1\ s^{-1}$) with a slope independent of the volume fraction: $\eta_\phi(\dot\gamma) \sim \dot\gamma^{n-1}$ where $n \in]1,2[$. In both cases the addition of particles has no impact on the value of the slope of both shear thinning and shear thickening behaviors. The shear thickening curve experimentally measured at $\phi = 40\%$ exhibits a lower slope at high $\dot\gamma$ values, which may be due to wall slipping.

The increase of volume fraction leads to an increase of the viscosity for all shear rates. In Fig. 2, the plateau viscosity (at $\dot\gamma \longrightarrow 0$) normalized by the viscosity at 0 % volume fraction is plotted as a function of the volume fraction for both suspensions, and those curves can be fitted with a "generalized" Krieger-Dougherty law which links the viscosity and the volume fraction (Krieger and Dougherty, 1959; Jarzebski, 1981) :

$$\eta_{KD}(\phi) = \eta_0(1 - \phi/\phi_{max})^{-n_{L,H}\phi_{max}} \tag{13}$$

where n_L and n_H are exponents in the low and high shear rate regimes, respectively. Also, ϕ_{max} is the maximum packing fraction and η_0 is a fitting parameter. For this analysis, we will rescale all low shear rate data such that $\eta_0 = 1$ (i.e. $\eta_0 = (\frac{\eta_\phi}{\eta_{\phi=0}})_{\dot\gamma\to 0}$). Note that, as mentioned in the introduction, while there are a variety of phenomenologically based formulas to fit such data, we found this form convenient. The original expression of Krieger-Dougherty may, moreover, be extended to the generalized Newtonian situation using the Jarzebski's approach (Jarzebski, 1981). However, the main results of this work do not depend on the specific formula chosen. The adjustments are performed by setting the value of ϕ_{max} equal to the random close packing concentration, 0.64. For the shear thinning suspension in the Newtonian regime (at $\dot\gamma = 0.5\ \mathrm{s}^{-1}$) the three parameters deduced from the fitting procedure are : $[\eta_0, \phi_{max}, n_L^{\mathrm{thin}}] = [1, 0.64, 2.84 \pm 0.12]$. For the shear thickening suspension at the Newtonian plateau the parameters values are $[\eta_0, \phi_{max}, n_L^{\mathrm{thick}}] = [1, 0.64, 4.06 \pm 0.32]$. For the shear thinning suspensions n_L is in agreement with the expected value (that is, the intrinsic viscosity equals $\frac{5}{2}$ for perfect spheres in the Newtonian regime). Conversely the n_L value for shear thickening suspensions, is much higher (4.07 ± 0.35).

The same regression analysis has been performed at high shear rates (at $\dot\gamma = 100$ for the shear thinning suspension and $\dot\gamma = 3\ \mathrm{s}^{-1}$ for the shear thickening suspension). For the shear thinning suspension we found $n_H^{\mathrm{thin}} = 1.47 \pm 0.07$, and we have $n_H^{\mathrm{thin}}/n_L^{\mathrm{thin}} = 0.52$ ($\approx .5$

for simulation). For the shear thickening suspension we obtain $n_H^{\text{thick}} = 6.11 \pm 0.30$, and $n_H^{\text{thick}}/n_L^{\text{thick}} = 1.51$ (≈ 1.8 for simulation). These values do not change significantly when the viscosities are taken at different shear rate values in the the generalized Newtonian regime. The ratio of the values of n_H and n_L for high and low shear rates are thus close to the exponent of the power law of the fluid medium (0.5 for the shear thinning and 1.5 for the shear thickening fluid) :

$$\frac{n_H}{n_L} \approx n \tag{14}$$

We will return to this point later. In addition it can be observed that the crossover between the two behaviors (at low and high shear rate) is shifted towards lower shear rate values as the volume fraction increases (Fig. 1). These two consequences of increasing volume fraction (the increase of the viscosity and the shift of the crossover position) are observed both for shear thinning and shear thickening suspensions. Therefore, the increase of the volume fraction only shifts the position of the curve in the log-log space viscosity *vs* shear rate : a homothetic transformation should be enough to superpose all the curves, and a scaling relationship exists between the viscosities at different volume fractions:

$$\frac{\eta_\phi(\dot\gamma)}{\eta_{sc}(\phi)} = \eta_{\phi_0}\left(\frac{\dot\gamma}{\dot\gamma_{sc}(\phi)}\right) \tag{15}$$

where $\eta_{sc}(\phi)$ and $\dot\gamma_{sc}(\phi)$ are dimensionless scaling parameters. If a power-law fluid medium is assumed so that $\eta_\phi(\dot\gamma,\phi) = A_\phi\dot\gamma^{n-1}$ (A_ϕ is a constant with units Pa s^n):

$$\frac{A_\phi\dot\gamma^{n-1}}{\eta_{sc}(\phi)} = A_{\phi_0}\left(\frac{\dot\gamma}{\dot\gamma_{sc}(\phi)}\right)^{n-1} \tag{16}$$

$$\frac{A_\phi}{\eta_{sc}(\phi)} = \frac{A_{\phi_0}}{\dot\gamma_{sc}(\phi)^{n-1}} \tag{17}$$

$$A_\phi = \left(\frac{\eta_{sc}(\phi)}{\dot\gamma_{sc}(\phi)^{n-1}}\right)A_{\phi_0} \tag{18}$$

The reference curve chosen for this example is the fluid medium curve ($\phi_0 = 0\%$). We apply a least-square regression to superpose a given curve, at volume fraction ϕ , with the flow curve of the suspending fluid. In a first step, the experimental points are fitted with a power-law fluid previously described to increase the accuracy of the least-squares method. Then the difference between fitting curves at different volume fractions is minimized using a least-square algorithm. One obtains values for both shear rate and viscosity scaling

parameters $\dot{\gamma}_{sc}$ and η_{sc} that minimize the difference between the reference curve and the scaled one. The superpositions of both shear thinning and shear thickening flow curves are plotted in Fig. 3 . Considering the number of curves and the experimental uncertainty, the superposition of both suspensions is remarkable and enables one to conclude in favor of the existence of a universal scaling that accounts for the increase of the volume fraction in a suspension. The discrepancy between the simulations and the experiments with 100 μm diameter particles at low shear rates may be attributed to the fact that the shear thinning behavior of the corn starch suspension at low shear rates is not taken into account by the constitutive law of the fluid medium used in the simulations (see also Fig. 1).

The flow curves may also be rescaled using a unique scaling parameter, $H(\dot{\gamma})$, following the procedure by Gleissle and Hochstein (2003) : a stress value is chosen, and $H(\dot{\gamma})$ is defined so that all the shifted curves superpose at this value (Fig. 4). A discrepancy is then obtained at low and high shear rate values. The error between the rescaled curves and the matrix fluid, ϵ_s, may be defined as the average of the euclidean distances in the $(\log(\dot{\gamma}), \log(\eta))$ plane between each point of the shifted flow curve, P_i^{shift} and the continuous matrix flow curve :

$$\epsilon_s(\phi) = \frac{1}{N} \sum_i d(P_i^{\text{shift}}(\phi), \log \eta_0(\log \dot{\gamma})) \tag{19}$$

where $P_i^{\text{shift}}(\phi)$ is a shifted point of the flow curve at volume fraction ϕ and N the total number of shifted points. The error in the superposition with two scaling factors is at least twice as small as the errors with a unique scaling factor, $H(\dot{\gamma})$.

The dimensionless scaling factors $\dot{\gamma}_{sc}$ and η_{sc} are plotted as a function of the volume fraction in Fig. 5 for both suspension families, and compared to the scaling factors deduced from the data of Lin *et al* (Lin *et al.*, 2014). The viscosity scaling parameter, η_{sc}, increases with the volume fraction as it has been observed previously and consistently with the Krieger-Dougherty theory, meanwhile the shear rate shift factor $\dot{\gamma}_{sc}$ decreases with the volume fraction. Those observations are satisfied for both shear thinning and shear thickening suspensions. For the shear thinning fluid, where the behavior of the matrix is well rendered over the entire shear rate range, superposition between experiments and simulations is observed. For all the volume fractions studied, the viscosity shift is higher for the shear thickening suspension ($\eta_{sc}^{\text{thick}} > \eta_{sc}^{\text{thin}}$) meanwhile the shear rate shift is lower $\dot{\gamma}_{sc}^{\text{thick}} \leq \dot{\gamma}_{sc}^{\text{thin}}$

and thus there is a difference in terms of shift factors between shear thinning and shear thickening suspension. As a conclusion, the scaling factors depend on the exponent of the constitutive law that describes the fluid.

Using the generalized Krieger-Dougherty relationship (Eq. 13), one can estimate the evolution of $\dot{\gamma}_{sc}$ and η_{sc} as a function of ϕ. Let us call n the exponent of the power-law fluid in the high shear rate regime, $\eta \sim \dot{\gamma}^{n-1}$. The scaling parameters can be related by considering the asymptopic behavior of the viscosity versus shear rate curves.

At low shear rates we assume that the viscosity is independent of shear rate.

$$\eta_{NNL}^{KD}(\phi) = \left(1 - \frac{\phi}{\phi_{max}}\right)^{-n_L \phi_{max}} \tag{20}$$

For simplicity it is assumed that the fluid medium viscosity is normalized to 1. The subscript L corresponds to the low shear rate regime. At the high shear rate regime we fit data to :

$$\eta_{NNH}^{KD}(\phi, \dot{\gamma}) = A_0 \dot{\gamma}^{n-1} \left(1 - \frac{\phi}{\phi_{max}}\right)^{-n_H \phi_{max}} \tag{21}$$

$$\tag{22}$$

where A_0 is a constant describing the fluid medium at high shear rates and n_H is a fitting parameter. The subscript H refers to the high shear rate regime.

Each of these two equations represent the viscosity in their separate regimes but cannot account for the other. Indeed, if we divide the entire data set by the low shear rate form the high shear rate data will not collapse on the same curve. However, we can correct for that by using the scaling parameter $\dot{\gamma}_{sc}$ for each volume fraction, according to Eq. 15 such that all data collapse onto the fluid medium viscosity in the high shear rate limit. That is :

$$\frac{\eta_{NNH}^{KD}(\phi, \dot{\gamma}_{sc}\dot{\gamma})}{\eta_{NNL}^{KD}(\phi)} = A_0 \dot{\gamma}^{n-1} \tag{23}$$

Solving for $\dot{\gamma}_{sc}$

$$\dot{\gamma}_{sc} = \left(1 - \frac{\phi}{\phi_{max}}\right)^{-\phi_{max} \frac{n_H - n_L}{n-1}} = \eta_{sc}^{-\frac{\frac{n_H}{n_L} - 1}{n-1}} \tag{24}$$

$$\tag{25}$$

Using the relationship between the Krieger-Dougherty exponents at low and high shear rates (Eq. 14), n being the exponent of the power-law fluid, we have :

$$\eta_{sc} = 1/\dot{\gamma}_{sc} \tag{26}$$

The Krieger-Dougherty relationships, in the Newtonian and generalized Newtonian regime thus predict a simple relation between the viscosity and the shear rate shifts. This relation is rigorously equivalent to stating that all the flow curves superimpose when plotted as $\eta(\sigma)$, as it is demonstrated by Highgate and Whorlow (1970) and Barnes (2003). Using the ϕ_{max} and the n_L values obtained by fitting the curves at low shear rate, we compute η_{sc} as a function of the volume fraction because η_{sc} is only the ratio between the viscosity at a given volume fraction and the viscosity at zero volume fraction. The ϕ_{max} for shear thinning and shear thickening being identical, η_{sc} is the same for both fluids. Then using the relationship obtained in Eq. 25, $\dot{\gamma}_{sc}$ is computed. These shifts are plotted in Fig. 4 **(a)** and **(b)** (continuous and dashed lines). Although the evolution of η_{sc} and $\dot{\gamma}_{sc}$ as a function of the volume fraction are roughly consistent with Krieger-Dougherty behavior, the simple relation $\eta_{sc} = 1/\dot{\gamma}_{sc}$ is not satisfied, neither by the experiments nor by the simulations (Fig. 4 **(c)**). This is due to the fact the values of $\dot{\gamma}_{sc}$ are underestimated by the Krieger-Dougherty model.

The inverse relationship between η_{sc} and $\dot{\gamma}_{sc}$(Eq. 25) may be expected on a physical point of view by looking at the equilibrium of a slice of fluid located between the coordinate z and $z + dz$, where the axis z is oriented along the vorticity axis (Barnes, 2003). Under steady state, assuming that the flow is Couette-like and the system homogeneous, the Navier-Stokes equation implies that the tangential stresses acting on faces parallel to the flow equilibrate : $\sigma_x(z) = \sigma_x(z + dz)$. As a consequence, σ_x is homogeneous everywhere in the sample (Barnes, 2003), and the transition between the Newtonian and the generalized Newtonian regime should occur at the same tangential stress for all volume fractions. This is equivalent to saying that η_{sc} and $\dot{\gamma}_{sc}$ are linked by Eq. 25. Conversely, we observe that the viscosity scaling parameter is larger than the inverse of the shear rate scaling parameter (Fig. 4**(c)**). This implies that the conditions for stress homogeneity are not satisfied as the local shear rates may be highly fluctuating due to the presence of the particles. A possible mechanism for the transportation of momentum out of a slice parallel to the flow is the

motion of particules out of the planes normal to the vorticity, whose contribution increases with the volume fraction of the suspension, as shown by Sierou and Brady (2002).

In order to have access to these spatial heterogeneities, we perform numerical simulations, looking for scaling properties of the local quantities of the flow. In particular, we will study the local shear rates ; we will show that their density of probability possesses scaling properties that can be related to the macroscopic scaling parameters of the flow curves, η_{sc} and $\dot{\gamma}_{sc}$.

IV. LOCAL SHEAR RATE DISTRIBUTION

We next present numerical simulation results of the microscopic flow fields to better understand the basis of the rescaling ansatz (Eq. 18). Denote σ and $\dot{\gamma}$ as the macroscopic values of the stress and shear rate, whereas their local values, as computed from numerical simulations are σ_l and $\dot{\gamma}_l$.

In the SPH-based simulations, we distinguish between stresses arising from the SPH "fluid medium" particles and stresses between spheres near contact due to lubrication forces. The macroscopic stress, σ, is the sum of the stresses over all SPH particles (σ^{SPH}) and over all sphere contacts, (σ^c). The relative contribution of the SPH particles and of the contacts to the overall stress are respectively $\Phi^{SPH} = \sigma^{SPH}/\sigma$ and $\Phi^c = \sigma^c/\sigma$. We also define the corresponding probability density functions for the local shear rates, $P^{SPH}_{\phi,\dot{\gamma}}(\dot{\gamma}_l)$ and $P^{c}_{\phi,\dot{\gamma}}(\dot{\gamma}_l)$: due to the wide range of $\dot{\gamma}_l$ we use a logarithmic scale for all the distributions which will be discussed in the following paragraphs, thus the step length between two points of a distribution is constant, C, on a logarithmic scale ($\forall i,\ \ln(i+1) - \ln(i) = C$).

Whatever the nature of the suspending fluid, the relative contribution of the contacts to the macroscopic stress, Φ^c, increases when the volume fraction of the suspension increases, as shown in Fig. 6**(a)**. In addition, the relative contribution of the spheres in contact to the macroscopic stress depends on the nature of the fluid and is higher for shear thickening suspensions.

The average stress *per* SPH particle (σ^{SPH} divided by the number of SPH particles) for the shear thinning suspensions are given in Table I. This represents the contribution of

the SPH particles to the overall stress. It increases with the shear rate but, surprisingly, does not change significantly when the volume fraction increases. By contrast, the relative contribution of the SPH particles to the macroscopic stress diminishes when the volume fraction increases, due to the increase in the number of inter-sphere contacts (Fig. 6**(b)**) and to the higher local shear rate at these contacts.

Volume Fraction	$\dot{\gamma}$ (s^{-1})			
	1	3	10	30
20 %	0.0096	0.0266	0.0583	0.1129
40 %	0.0117	0.0304	0.0652	0.1253
50 %	0.0117	0.0294	0.0620	0.1311

TABLE I. Average stress associated with SPH particles for shear thinning suspensions

We now make some qualitative observations regarding the shear rate probability density to construct a general expression for $P^{SPH}_{\phi,\dot{\gamma}}(\dot{\gamma}_l)$ and $P^{c}_{\phi,\dot{\gamma}}(\dot{\gamma}_l)$. The probability densities $P^{SPH}_{\phi,\dot{\gamma}}(\dot{\gamma}_l)$ and $P^{c}_{\phi,\dot{\gamma}}(\dot{\gamma}_l)$ exhibit different characteristic shapes (Fig. 7). It is observed that the shear rate distribution of SPH particles is centered around the macroscopic shear rate, $\dot{\gamma}$, whereas the contact shear rate distribution spreads over several orders of magnitude of $\dot{\gamma}_l$. On the other hand, the general shape of the probability density functions are not significantly modified by the applied macroscopic shear rate. Comparing shear rate distributions of the contacts of both 20% and 50% volume fraction, it can be observed that the increase of the volume fraction reduces the low shear rate population and increases the high shear rate population. While the contacts at high shear rate produce large values of the local stress σ_l, the probability of a high-sheared contact is very low. Therefore in order to be more quantitative, the value of the stresses deduced from both shear rate distributions will be calculated and compared. For the rest of the study, we consider $\dot{\gamma} = 2\dot{\gamma}^*$, corresponding to $\dot{\gamma} = 10\ s^{-1}$ for the shear thinning matrix and $\dot{\gamma} = 3\ s^{-1}$ for the shear thickening matrix.

We observe (Fig. 7 **(a)**) that, at the same volume fraction, the shear rate distributions are remarkably similar for shear thinning, Newtonian and shear thickening fluid media. This feature of the local shear rates may, in part, be due to the application of a constant applied rate of strain at the cell boundaries, so that the mean flow approaches that of Couette flow

over long enough time. For the case when volume fraction is allowed to vary (Fig. 7 **(b)**), the SPH particles and contacts shear rate distributions separately remain similar in shape but one can see that increasing the volume fraction (i) increases the contacts probability density at high shear rates and (ii) increases the tail of the fluid medium probability density at high shear rates.

In summary, for different volume fractions (at same shear rate) the simulation data for local contact shear rates can approximately collapse on same curve by rescaling the shear rate. Therefore the general scaling law for the probability density of the contact shear rates should be of the form :

$$P^c_{\phi,\dot{\gamma}}(\dot{\gamma}_l) = \frac{1}{\alpha^c_{\phi,\phi_0}} P^c_{\phi_0,\dot{\gamma}} \left(\frac{\dot{\gamma}_l}{\alpha^c_{\phi,\phi_0}} \right) \tag{27}$$

For the SPH fluid particles, the probability density is centered at $\dot{\gamma}_l = \dot{\gamma}$, and a similar scaling behavior can be written taking $\dot{\gamma}_l - \dot{\gamma}$ as the variable. Thus, one can modify the previous general scaling laws for the probability density of the SPH shear rates :

$$P^{SPH}_{\phi,\dot{\gamma}}(\dot{\gamma}_l - \dot{\gamma}) = \frac{1}{\alpha^{SPH}_{\phi,\phi_0}} P^{SPH}_{\phi_0,\dot{\gamma}} \left(\frac{\dot{\gamma}_l - \dot{\gamma}}{\alpha^{SPH}_{\phi,\phi_0}} \right) \quad \text{for } \dot{\gamma}_l > \dot{\gamma} \tag{28}$$

This law does not allow for the rescaling of the shear rate probability density at low shear rates. Nevertheless the weakly sheared SPH particles do not significantly contribute to the total stress.

The scaling factors α^c_{ϕ,ϕ_0} and $\alpha^{SPH}_{\phi,\phi_0}$ may be related to the average values of the local shear rates :

$$< \dot{\gamma}_l >^c_{\phi,\dot{\gamma}} = \int_{-\infty}^{\infty} P^c_{\phi,\dot{\gamma}}(\dot{\gamma}_l) \dot{\gamma}_l d\dot{\gamma}_l \tag{29}$$

$$= \int_{-\infty}^{\infty} \frac{1}{\alpha^c_{\phi,\phi_0}} P^c_{\phi_0,\dot{\gamma}} \left(\frac{\dot{\gamma}_l}{\alpha^c_{\phi,\phi_0}} \right) \dot{\gamma}_l d\dot{\gamma}_l \tag{30}$$

$$= \alpha^c_{\phi,\phi_0} \int_{-\infty}^{\infty} P^c_{\phi_0,\dot{\gamma}}(u) u du \tag{31}$$

$$= \alpha^c_{\phi,\phi_0} \langle \dot{\gamma}_l \rangle^c_{\phi_0,\dot{\gamma}} \tag{32}$$

$$\alpha^c_{\phi,\phi_0} = \frac{\langle \dot{\gamma}_l \rangle^c_{\phi,\dot{\gamma}}}{\langle \dot{\gamma}_l \rangle^c_{\phi_0,\dot{\gamma}}} \tag{33}$$

where $\langle ... \rangle^c$ denotes the average over the contact shear rate distribution.

A similar relationship may be obtained, that relates $\alpha^{SPH}_{\phi,\phi_0}$ to the shear rate averages :

$$\alpha^{SPH}_{\phi,\phi_0} = \frac{\langle \dot{\gamma}_l - \dot{\gamma} \rangle^{SPH}_{\phi,\dot{\gamma}}}{\langle \dot{\gamma}_l - \dot{\gamma} \rangle^{SPH}_{\phi_0,\dot{\gamma}}} \quad \text{for } \dot{\gamma}_l > \dot{\gamma} \tag{34}$$

The rescaled SPH shear rate probability densities are plotted in Fig. 8 using the value of α^{SPH} deduced from Eq. 34. A good superposition is obtained for local shear rates larger than the macroscopic shear rate, between different fluids behavior **(a)** and at different volume fractions for a given fluid **(b)**. The evolution of α^{SPH} as a function of the volume fraction is given in Fig. 10. The scaling factors are identical for the shear thinning and the shear thickening suspensions.

The rescaling of the contact shear rate distributions is illustrated in Fig. 9 where the contact scaling parameter α^c utilized was determined from Eq. 33 and shown in Fig. 10. Once again, there is a good superposition for local shear rate for the volume fraction and the fluid media studied. Surprisingly, the contact scaling factors for shear thinning suspensions are equal to those obtained for the rescaling of the SPH shear rate distributions. In contrast, the contact scaling factors for the shear thickening suspensions are larger at high volume fraction when compared to the SPH scaling factors.

To conclude, we are able, using the scaling law defined in Eq. 27 and 28, (i) to calculate two microscopic scaling parameters α^{SPH} and α^c respectively for SPH and contact shear rate distributions, (ii) to use those parameters to obtain, whatever the volume fraction and the fluid medium, a master curve for both shear rate distributions.

Would the particles move along flow lines parallel to the macroscopic shear rate, the α coefficients would be of purely geometric origin : the interparticle distance decreases when the volume fraction increases. This induces an increase of the local shear rate. This increase would then be simply related to the macroscopic shear rate shift factor, $\dot{\gamma}_{sc}$ and we should observe that :

$$\alpha_{\phi,\phi_0} \sim \frac{1}{\dot{\gamma}_{sc}} \tag{35}$$

Nevertheless, under such assumptions (particles moving along flow lines parallel to the macroscopic shear rate), the stress continuity would be guaranteed, and we would observe that $\eta_{sc} \sim 1/\dot{\gamma}_{sc}$. We have seen that this is not the case, and we shall now look for a more general relationship between α_{ϕ,ϕ_0} and the macroscopic shift factors.

We have shown that both the macroscopic flow curves $\sigma(\dot{\gamma})$ and the local shear rate distributions may be rescaled onto master curves measured at a chosen volume fraction. We have defined several macroscopic scaling parameters : $\eta_{sc}(\phi)$ and $\dot{\gamma}_{sc}(\phi)$ on one hand and microscopic scaling parameters: α^{SPH} and α^c on the other hand. We now seek to relate these parameters. More precisely, we look for a relationship between the macroscopic parameters and α^c.

The mean value of the stress arising from the contacts can be expressed as the stress resulting from the contacts between particles and divided by the number of contacts or by calculating it directly from the shear rate distribution :

$$< \sigma >^c_{\phi,\dot{\gamma}} = \int_{-\infty}^{\infty} P^c_{\phi,\dot{\gamma}}(\dot{\gamma}_l)\eta(\dot{\gamma}_l)\dot{\gamma}_l d\dot{\gamma}_l \tag{36}$$

In the following derivation, Eq. 27 and a power law for the fluid will be used. The power law is justified by the fact that almost all the shear rate contributing to the stress is located at high shear rates so that the following approximation can be used :

$$\langle\sigma\rangle^c_{\phi,\dot{\gamma}} = \int_{-\infty}^{\infty} \frac{1}{\alpha^c_{\phi,\phi_0}} P^c_{\phi_0,\dot{\gamma}}\left(\frac{\dot{\gamma}_l}{\alpha^c_{\phi,\phi_0}}\right)\eta(\dot{\gamma}_l)\dot{\gamma}_l d\dot{\gamma}_l \tag{37}$$

$$= \int_{-\infty}^{\infty} \frac{1}{\alpha^c_{\phi,\phi_0}} P^c_{\phi_0,\dot{\gamma}}\left(\frac{\dot{\gamma}_l}{\alpha^c_{\phi,\phi_0}}\right) A_0\dot{\gamma}_l^{n-1}\dot{\gamma}_l d\dot{\gamma}_l \tag{38}$$

$$= (\alpha^c_{\phi,\phi_0})^n \int_{-\infty}^{\infty} P^c_{\phi_0,\dot{\gamma}}(u) A_0 u^{n-1} u du \tag{39}$$

$$= (\alpha^c_{\phi,\phi_0})^n \int_{-\infty}^{\infty} P^c_{\phi_0,\dot{\gamma}}(u)\eta(u) u du \tag{40}$$

$$\langle\sigma\rangle^c_{\phi,\dot{\gamma}} = (\alpha^c_{\phi,\phi_0})^n \langle\sigma\rangle^c_{\phi_0,\dot{\gamma}} \tag{41}$$

Therefore mean values of stresses arising from the contacts at different volume fractions can be related using the parameter α^c_{ϕ,ϕ_0}. Knowing the relative proportion of the stress coming from the contact, $\Phi^c(\phi)$, and the number of contacts in the sample, $N^c(\phi)$ (Fig. 6), the total stress at volume fraction ϕ is now related to the average contact stress $\langle\sigma\rangle^c_{\phi,\dot{\gamma}}$.

$$\langle\sigma\rangle^c_{\phi,\dot{\gamma}} = \frac{1}{N^c(\phi)}\sigma^{c,total}_{\phi,\dot{\gamma}} = \frac{\Phi^c(\phi)}{N^c(\phi)}\sigma_{\phi,\dot{\gamma}} \tag{42}$$

We thus have :

$$\frac{\Phi^c(\phi)}{N^c(\phi)}\sigma_{\phi,\dot{\gamma}} = (\alpha^c_{\phi,\phi_0})^n \frac{\Phi^c(\phi_0)}{N^c(\phi_0)}\sigma_{\phi_0,\dot{\gamma}} \tag{43}$$

$$\sigma_{\phi,\dot{\gamma}} = (\alpha^c_{\phi,\phi_0})^n \frac{\Phi^c(\phi_0)N^c(\phi)}{\Phi^c(\phi)N^c(\phi_0)}\sigma_{\phi_0,\dot{\gamma}} \tag{44}$$

Combining both equations 18 and 44, that relate the value of stress at different volume fractions using, macroscopic and microscopic parameters respectively, one has :

$$\frac{\eta_{sc}(\phi)}{\dot{\gamma}_{sc}(\phi)^{n-1}} = (\alpha^c_{\phi,\phi_0})^n \frac{\Phi^c(\phi_0)N^c(\phi)}{\Phi^c(\phi)N^c(\phi_0)} \tag{45}$$

$$\frac{\eta_{sc}(\phi)}{\dot{\gamma}_{sc}(\phi)^{n-1}} = (\alpha^c_{\phi,\phi_0})^n f(\phi,\phi_0) \tag{46}$$

Providing a relationship between the microscopic and the macroscopic shift parameters. This relation involves the fraction of stress arising from the contacts and the number of contacts. We have observed that both the number of contacts, and the fraction of stress from contacts increases with the volume fraction in a similar way, leading to :

$$\frac{\eta_{sc}(\phi)}{\dot{\gamma}_{sc}(\phi)^{n-1}} \approx (\alpha^c_{\phi,\phi_0})^n \tag{47}$$

which corresponds to the stress continuity approximation (Eq. 35).

In Fig. 11, the left and right part of Eq. 46 have been plotted as a function of the volume fraction, using the $\phi = 20$ % flow curve as the reference curve. We indeed obtain a correlation between the parameters α, η_{sc}, and $\dot{\gamma}_{sc}$ for both shear thinning and shear thickening suspensions demonstrating the relevance of our approach.

V. CONCLUSION

We have demonstrated that viscosity *vs* shear rate curves for suspensions with a wide range of volume fraction and having the same fluid medium can be collapsed onto a single universal curve describing the fluid medium. For the systems studied two scaling parameters were identified that depend on the volume fraction and the asymtopic behavior of the fluid

medium at low and high shear rates. Furthermore, the scaling parameters are linked by the width of the distribution of microscopic shear rates.

For a pure Newtonian fluid, the increase of the viscosity with the volume fraction is generally described by the Krieger-Dougherty equation. However, for a case of a generalized Newtonian fluid which makes a transition from a Newtonian to a power-law behavior, a second parameter is needed to collapse the data onto the matrix constitutive equation. This second scaling parameter is hidden unless there is a change in the rheological behavior of the matrix fluid. The existence of two different macroscopic scaling parameters is a direct consequence of stress heterogeneity due to contacts inside the sample. This is true both for shear-thinning and shear-thickening suspending fluids. Remarkably, when the volume fraction of the suspension increases, most of the local shear rates do not increase, but only those corresponding to small interparticle distances (Fig. 6). As a consequence, the overall stress is dominated by the stress between particles close to contact. We found that the product of the scaling parameters is approximately equal to 1. As we go to higher volume fractions, and the contribution of the contacts increases, the product value further departs from 1. This can be illustrated by a toy model : assuming that η_{sc} is controlled by Krieger-Dougherty at low shear rates, and that $\dot{\gamma}_{sc}$ is given by the average value of the local shear rates, $\dot{\gamma}_l$, in the suspending medium. Let us approximate the local shear rates as $\dot{\gamma}\frac{d(\phi)}{d(\phi)-2R}$, $\dot{\gamma}$ being the macroscopic shear rate, $d(\phi)$ the average distance between two neighbor particles center and R their radius, in between neighbor particles and $\dot{\gamma}$ everywhere else in the suspending fluid. One easily shows that the volume average of the local shear rate does not increase as rapidly as the Newtonian viscosity. As a result, $\eta_{sc}\dot{\gamma}_{sc} > 1$. This result may be understood as a consequence of the increasing contribution of the highest shear rates to the macroscopic values of viscosity when the volume fraction increases.

Finally, by determining the constitutive relation of the fluid medium through experiment and having information of the volume fraction one may predict the constitutive relation (viscosity *vs* shear rate) of a suspension. Such a result is useful because measuring the properties of the fluid medium are, generally, much easier and more accurate than that of the suspension. Consequently, fewer tests would then be needed to determine a suspension's rheological properties.

VI. ACKNOWLEDGEMENTS

We would like to thank Kenneth Snyder for carefully reading this paper and making many useful comments. This research used resources of the Argonne Leadership Computing Facility at Argonne National Laboratory, which is supported by the Office of Science of the U.S. Department of Energy under contract DE-AC02-06CH11357.

VII. APPENDIX

Proper construction of the weight function $W(r)$ is important for the physically correct transmission of matter or forces between neighboring sph particles. Here some key properties of $W(r)$ and its derivative are given for convenience. The weight function and alternate formulations are discussed more fully in Español and Revenga (2003); Monaghan (2005).

$$\int d\mathbf{r} W(r) = 1. \tag{48}$$

$$\nabla W(r) = -\mathbf{r} F(r) \tag{49}$$

In this work the SPH (Monaghan, 2005) function, $W(r,h)$ is utilized for a weight function.

$$W(r,h) = \frac{105}{16\pi h^3}\left(1+3\frac{r}{h}\right)\left(1-\frac{r}{h}\right)^3 \tag{50}$$

and

$$F(r,h) = \left(\frac{315}{4\pi h^5}\right)\left(1-\frac{r}{h}\right)^2. \tag{51}$$

The parameter, h, describes a length scale that, for this work is set to $h = 1$. Some of the more important properties of $F(r)$ are given below.

$$\int d\mathbf{r} F(r)\mathbf{r}\mathbf{r} = \mathbf{1}. \tag{52}$$

$$\int d\mathbf{r} F(r)\frac{xxxx}{r^2} = \frac{3}{5}. \tag{53}$$

$$\int d\mathbf{r} F(r)\frac{xxyy}{r^2} = \frac{1}{5}. \tag{54}$$

DISCLAIMER

Certain commercial equipment, instruments, or materials are identified in this paper in order to specify the experimental procedure adequately. Such identification is not intended to imply recommendation or endorsement by the National Institute of Standards and Technology, nor is it intended to imply that the materials or equipment identified are necessarily the best available for the purpose.

REFERENCES

Allen M. and Tildesley D., *Computer simulations of liquids* (Clarendon, Oxford, 1987).

Barnes H., "A review of the rheology of filled viscoelestic systems." The British Society of Rheology, **22**, 1–36 (2003).

Batchelor G., *An Introduction to Fluid Dynamics* (Cambridge University Press, 1967).

Boek E., Coveney P., Lekkerkerker H., and van der Schoot P., "Simulating the rheology of dense colloidal suspensions using dissipative particle dynamics simulations," Physical Review E, **55**, 3124–3133 (1997).

Cheng Z., Zhu J., Chaikin P., Phan S.-E., and Russel W., "Nature of the divergence in low shear viscosity of colloidal hard-sphere dispersions." Physical Review E, **65**, 041405 (2002).

Cohen M. and Turnbull D., "Molecular transport in liquids and glasses," Journal of Chemical Physics, **31**, 1164–1169 (1959).

Dai S., Qi F., and Tanner R., "Viscometric functions of concentrated non-colloidal suspensions of spheres in a viscoelastic matrix," Journal of Rheology, **58**, 183–198 (2014).

Español P. and Revenga M., "Smoothed dissipative particle dynamics," Physical Review E, **67**, 026705 (2003).

Gleissle W. and Hochstein P., "Validity of the cox-merz rule for concentrated suspensions," Journal of Rheology, **47**, 897–910 (2003).

Götze W., *Liquids, Freezing, and the Glass Transition*, edited by J. Hansen, D. Levesque, and J. Zinn-Justin, Vol. 289-503 (Amsterdam, 1991).

Highgate D. and Whorlow R., "Rheological properties of suspensions of spheres in non-newtonian media," Rheologica Acta, 569–576 (1970).

Hoogerbrugge P. and Koelman J., "Simulating microscopic hydrodynamic phenomena with dissipative particle dynamics." Europhysics Letters, **19**, 155–160 (1992).

Jarzebski G., "On the effective viscosity of pseudoplastic suspensions." Rheologica Acta, **20**, 280–287 (1981).

Kataoka T., Kitano T., Sasahara M., and Nishijima K., "Viscosity of particle filled polymer melts." Rheologica Acta, **17**, 149–155 (1978).

Kim S. and Karrila S., *Microhydrodynamics* (Butterwort-Heinemann, 1991).

Krieger I. and Dougherty T., "A mechanism for non-newtonian flow in suspensions of rigid spheres." Transactions of the Society of Rheology, **III**, 137–152 (1959).

Landau L. and Lifshitz E., *Fluid Mechanic* (Pregamon Press, Oxford, 1987).

Lin Y., Phan-Thien N., and Khoo B., "Normal stress differences behavior of polymeric particle suspensions in shear flow," Journal of Rheology, **58**, 223–235 (2014).

Liu A. and Nagel S., *Jamming and Rheology, Constrained Dynamics on Microscopic and Macroscopic Scales* (Taylor and Francis, 2001).

Mall-Gleissle S., Gleissle W., McKinley G., and Buggisch H., "The normal stress behaviour of suspensions with viscoelastic matrix fluids," Rheologica Acta, **41**, 61–76 (2002).

Martys N., "Study of a dissipative particle dynamics based approach for modeling suspensions." Journal of Rheology, **49**, 401–424 (2005).

Martys N., George W., Chun B., and Lootens D., "A smoothed particle hydrodynamics-based fluid model with a spatially dependent viscosity: application to flow of a suspension with a non-newtonian fluid matrix," Rheologica Acta, **49**, 1059–1069 (2010).

Martys N. and Mountain R., "Velocity verlet algorithm for dissipative-particle-dynamics-based models of suspension," Physical Review E, **59**, 3733–3736 (1999).

Monaghan J., "Smoothed particle hydrodynamics," Reports on Progress in Physics, **68**, 1703–1759 (2005).

Roscoe R., "The viscosity of suspensions of rigid spheres," British Journal of Applied Physics, **3**, 267–269 (1952).

Sierou A. and Brady J., "Rheology and microstructure in concentrated noncolloidal suspensions," Journal of Rheology, **46**, 1031–1056 (2002).

Sundstrom D., "Viscosity of suspensions in polymeric solutions," Rheologica Acta, **22**, 420–423 (1983).

Tanner R., Dai S., Qi F., and Housiadas K., "Viscometric functions of semi-dilute non-colloidal suspensions of spheres in a viscoelastic matrix," Journal of Non-Newtonian Fluid Mechanics, **201**, 130–134 (2013a).

Tanner R., Qi F., and Dai S., "Scaling the normal stresses in concentrated non-colloidal suspensions of spheres," Rheologica Acta, **52**, 291–295 (2013b).

Tanner R., Qi F., and Housiadas K., "A differential approach to suspensions with power-law matrices." Journal of Non-Newtonian Fluid Mechanics, **165**, 1677–1681 (2010).

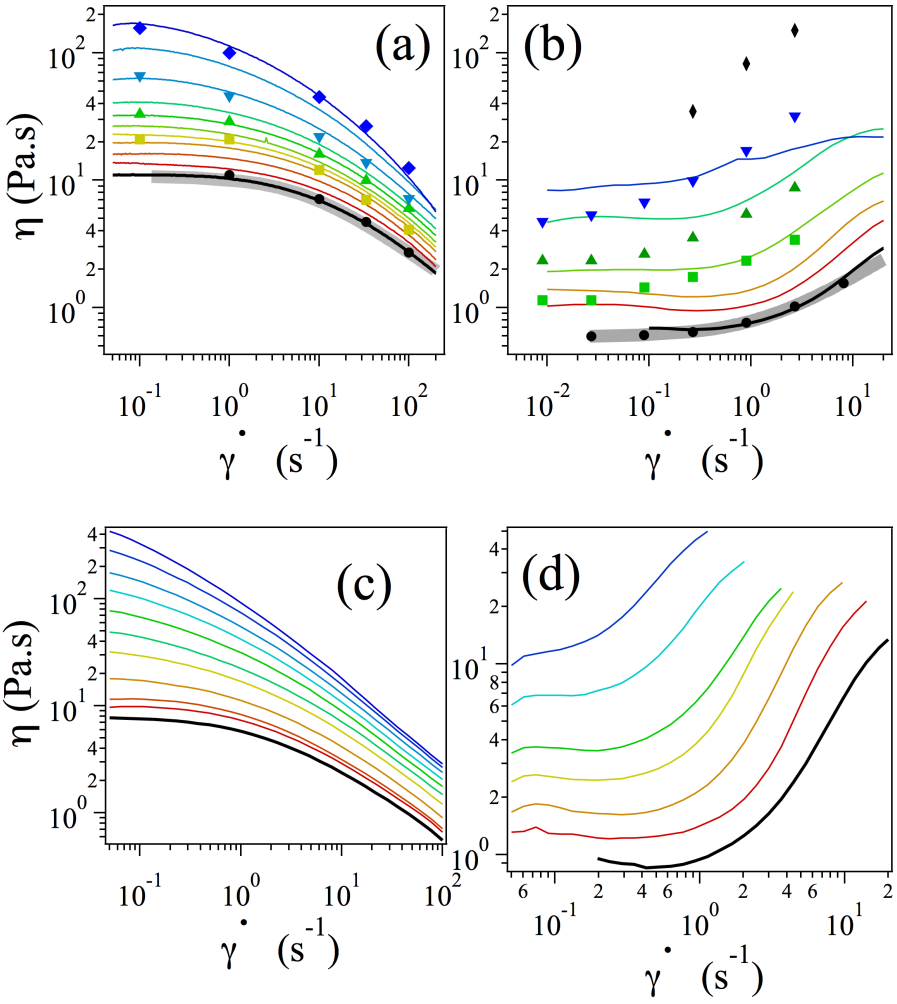

FIG. 1. Experimental (continuous lines) and simulated flow curves (large symbols) of suspensions in a shear thinning **(a)**, **(c)** and a shear thickening **(b)**, **(d)** fluid medium. The flow curve of the fluid medium used for the simulations is plotted in light grey. The experimentally measured concentrations for the shear thinning suspensions are : **(a)** 0 % (thick black continuous line), and, from red to blue, 5.5 %, 12 %, 18 %, 22 %, 26 %, 29 %, 34 %, 40 %, 45 % and 50 %. The SPH-simulations are performed at volume fractions of 0 % (•), 20 % (■), 30 % (▲), 40 % (▼) and 50 % (♦) and **(c)** : 0 % (black), and, from red to blue, 5 %, 10 %, 20 %, 30 %, 35 %, 40 %, 42.5 %, 45 %, and 47.5 %. For the shear thickening suspensions, the volume fractions used for experiments are **(b)** 0 % (thick black continuous line), 5 %, 10 %, 20 %, 30 % and 40 % and for simulations 0 % (•), 20 % (■), 30 % (▲) and 40 % (▼) and 50 % (♦). Experiments with 50 μm diameter particles **(d)** are performed at volume fractions equal to 0 %, 5 %, 10 %, 15 %, 20 %, 25 %, and 30 %.

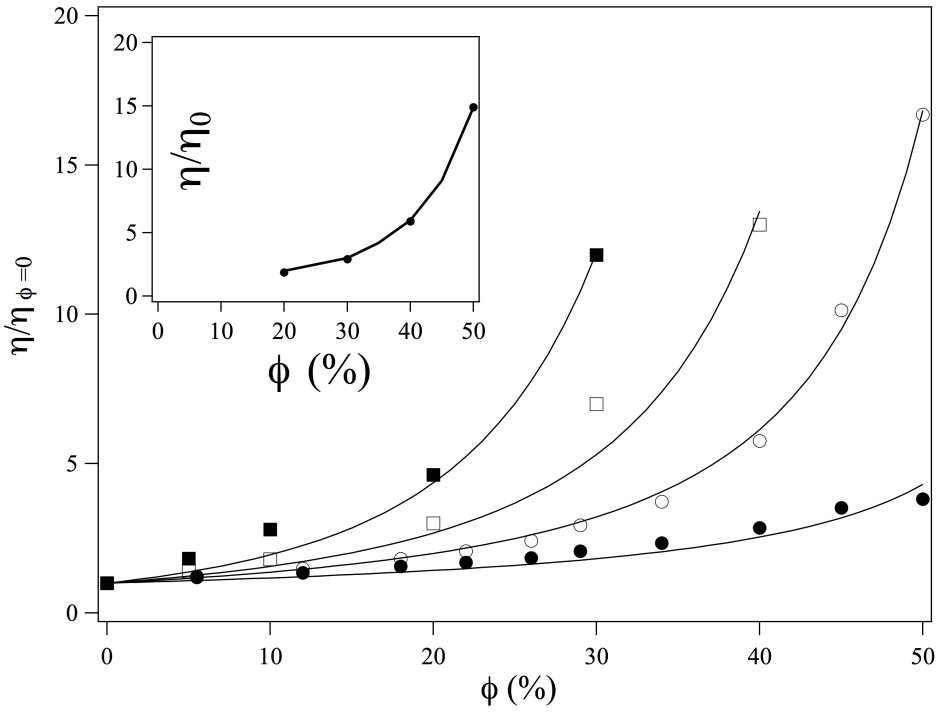

FIG. 2. Normalized viscosity at the plateau ($\dot{\gamma} \longrightarrow 0$) (empty symbols) and at high shear rate (full symbols) as a function of the volume fraction for the shear thinning (disk symbols) and shear thickening (square symbols) suspension. Fits are made using a Krieger-Dougherty model (Eq. 13). *Insert* Normalized viscosity obtained from the simulations (disks) are compared with the normalized viscosities of newtonian non-colloidal suspensions from Sierou and Brady (2002).

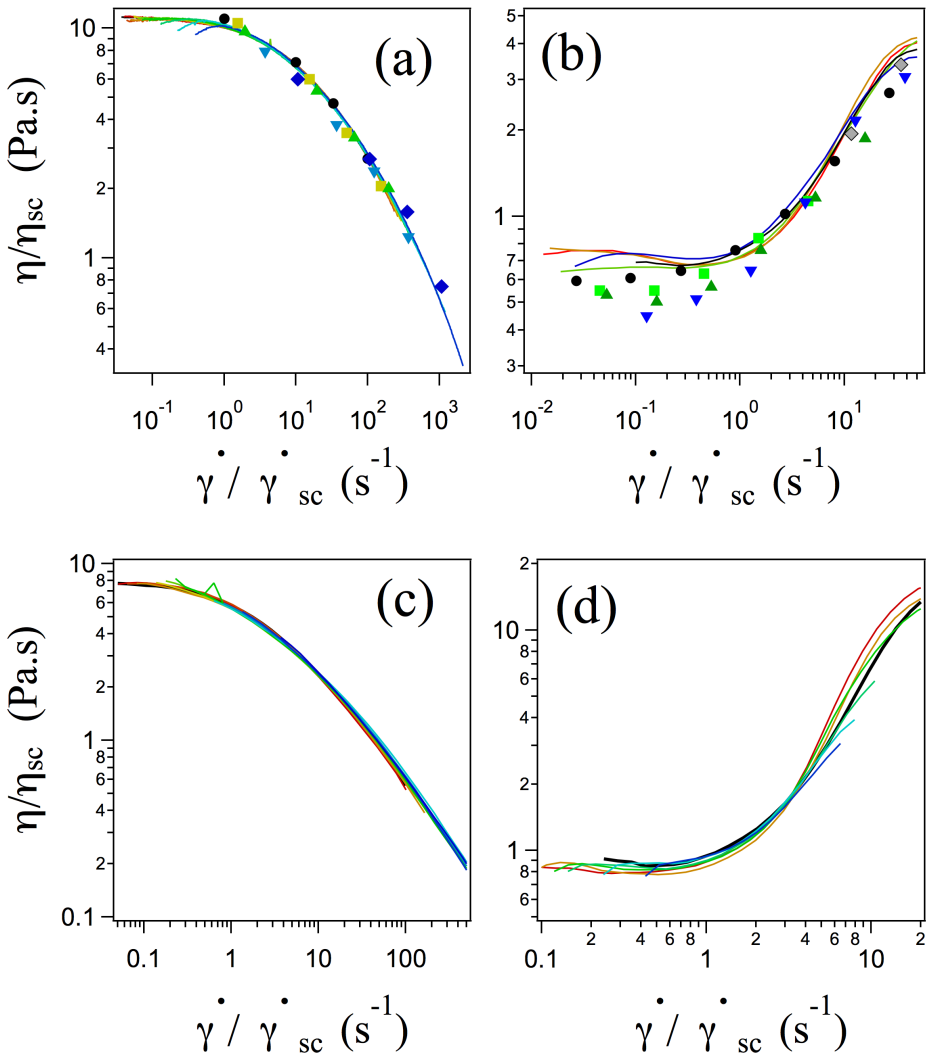

FIG. 3. Rescaled experimental (continuous lines) and simulated flow curves (large symbols) of suspensions in a shear thinning **(a)**, **(c)** and a shear thickening **(b)**, **(d)** fluid medium. The experimentally measured concentrations for the shear thinning suspensions **(a)** (100 μm diameter particles) are : 0 % (black), and, from red to blue, 5.5 %, 12 %, 18 %, 22 %, 26 %, 29 %, 34 %, 40 %, 45 % and 50 % and **(c)** (50 μm diameter particles) : 0 % (black), and, from red to blue, 5 %, 10 %, 20 %, 30 %, 30 %, 35 %, 40 %, 42.5 %, 45 %, and 47.5 % . The SPH-simulations **(a)** are performed at volume fractions of 0 % (•), 20 % (■), 30 % (▲), 40 % (▼) and 50 % (♦). For the shear thickening suspensions, volume fractions used for experiments are **(b)** 0 % (thick black continuous line), 5 %, 10 %, 20 %, 30 % and 40 % (experiments, 100 μm diameter particles) from red to blue and 0 % (•), 20 % (■), 30 % (▲) and 40 % (▼) (simulations). Experiments with 50μm diameter particles **(d)** are performed at volume fractions equal to 0 % (black), and, from red to blue, 5 %, 10 %, 15 %, 20 %, 25 %, and 30 %.

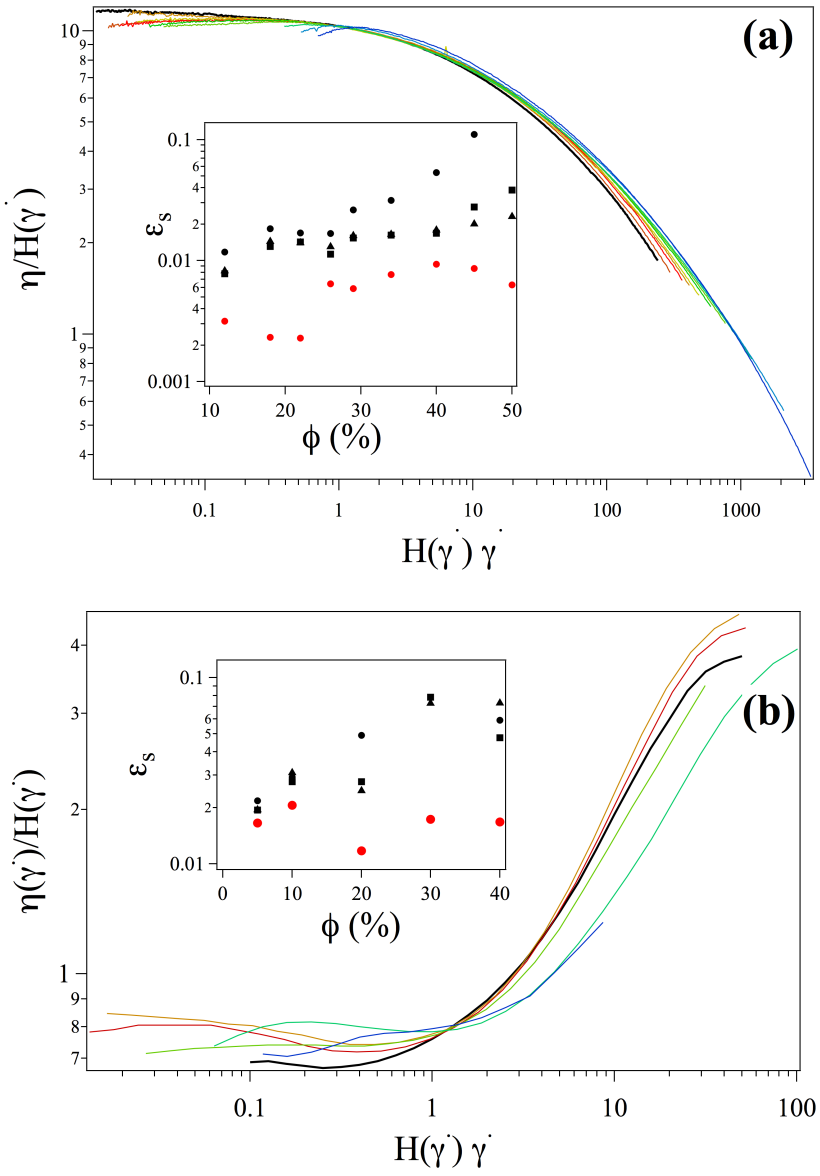

FIG. 4. Rescaled experimental flow curves with a unique scaling factor, $H(\dot{\gamma})$, of suspensions of 100 μm diameter particles in a shear thinning **(a)** and a shear thickening **(b)** fluid medium. The concentrations for the shear thinning suspensions **(a)** are : 0 % (black), and, from red to blue, 5.5 %, 12 %, 18 %, 22 %, 26 %, 29 %, 34 %, 40 %, 45 % and 50 %. For the shear thickening suspensions, volume fractions are **(b)** 0 % (thick black continuous line), 5 %, 10 %, 20 %, 30 % and 40 % from red to blue. *Insert :* Error between the shifted flow curves and the fluid matrix flow curve, ϵ_s, deined by Eq. 19. • : curves shifted with two scaling parameters η_{sc} and $\dot{\gamma}_{sc}$. Black symbols : flow curves are shifted using a single parameter, chosen so that the curves superimpose at $\sigma = 2$ Pa (•), $\sigma = 10$ Pa (■) and $\sigma = 50$ Pa (▲) for the shear thinning fluid and $\sigma = 0.2$ Pa (•), $\sigma = 1$Pa (■) and $\sigma = 5$ Pa (▲) for the shear thickening fluid.

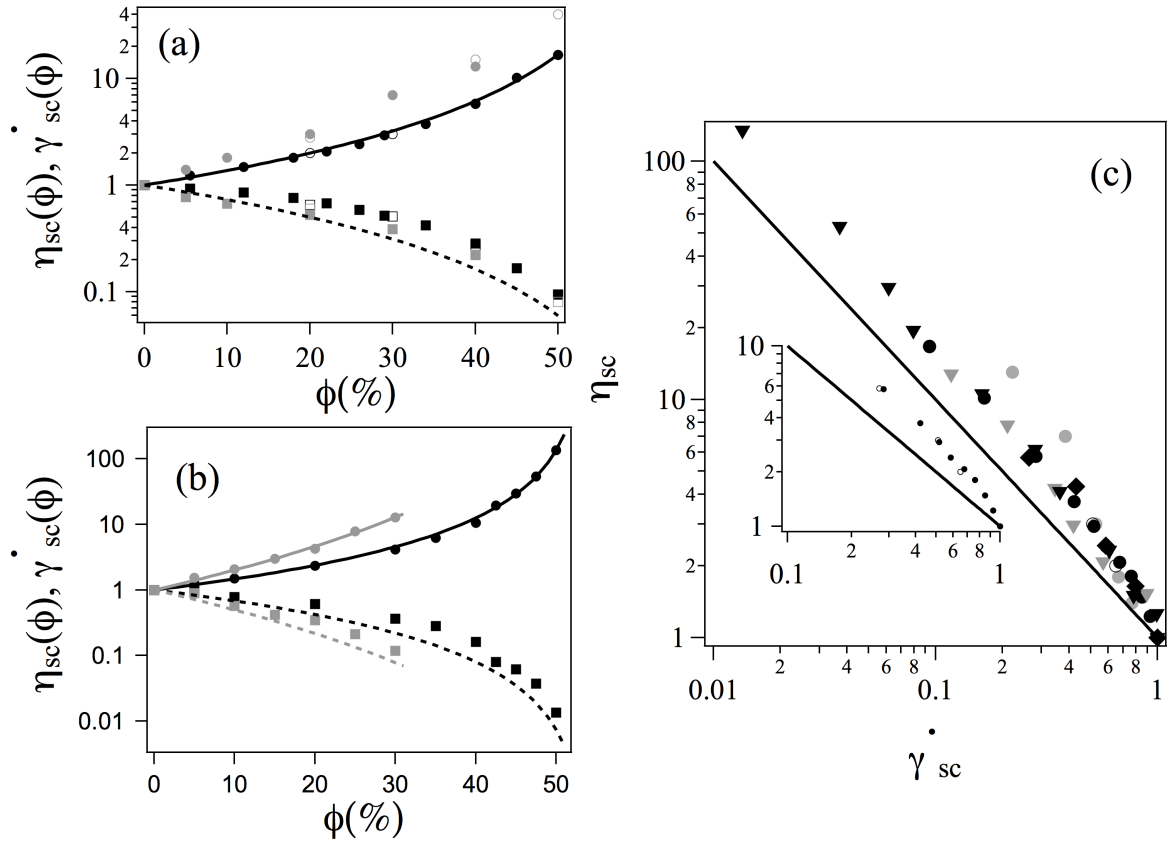

FIG. 5. **(a)** Evolution of η_{sc} (disks) and $\dot{\gamma}_{sc}$ (squares) as a function of the volume fraction ϕ for the 100 μm diameter **(a)** and 50 μm diameter **(b)** particles. Black symbols : shear thinning medium, grey symbols : shear thickening medium. Empty symbols are results from the simulations. Continuous lines are adjustments of η_{sc} obtained from the Krieger-Dougherty fluid-type equations (Eq. 20 and 26), $\eta^{KD}(\phi)$. Dashed lines are given by $1/\eta^{KD}(\phi)$. It should be noticed that the shear rate shift factor is underestimated. **(c)** Viscosity scaling factor as a function of the shear rate scaling factor for all the experiments and the simulations performed. Black disks : shear thinning matrix with 100 μm particles, grey disks : shear thickening matrix with 100 μm particles.. Black triangles : shear thinning matrix with 50 μm particles. Grey triangles : shear thickening matrix with 50 μm particles. Diamonds are data obtained from (Lin *et al.*, 2014). Continuous line represent the Krieger-Dougherty law (Eq. 26). *Inset :* Data for the shear thinning fluid only. Experiments : full symbols, simulations : empty symbols.

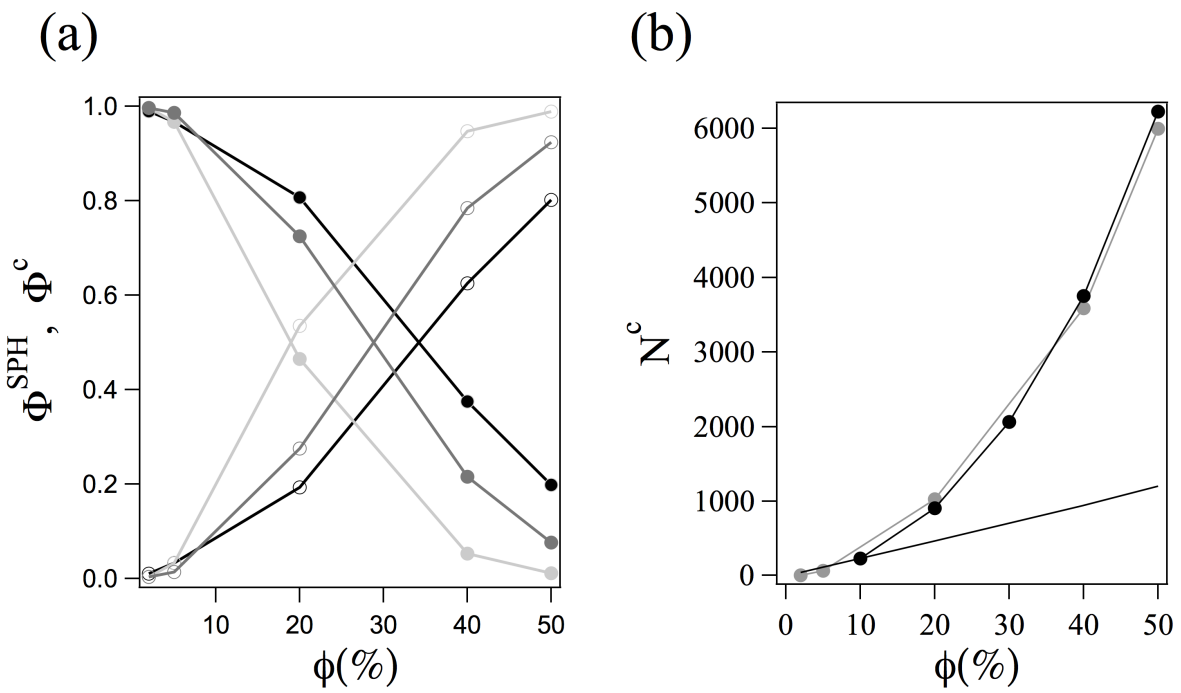

FIG. 6. **(a)** Relative contribution of stress due to SPH particles Φ^{SPH} (full disks) and contact stress, Φ^c (empty circles) to the macroscopic stress, as a function of the volume fraction for shear thinning (black symbols), Newtonian (medium grey symbols) and shear thickening (light grey symbols), under shear rate $\dot{\gamma} = 30$ s^{-1}. **(b)** Number of contacts, N^c as a function of the volume fraction for the shear thinning (black disks) and shear thickening suspensions (grey disks), at $\dot{\gamma} = 30$ s^{-1}. The straight line indicates the number of spheres as a function of the volume fraction.

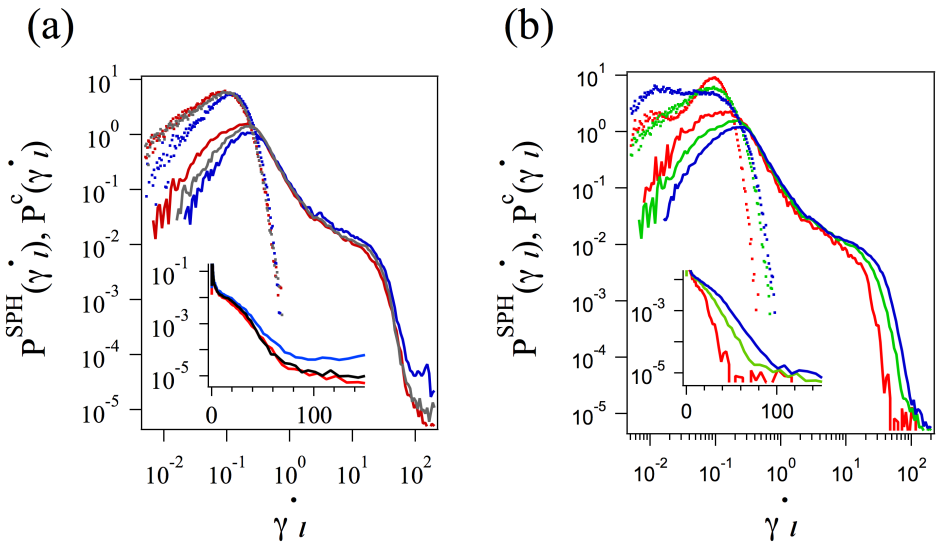

FIG. 7. **(a)** Probability density of local shear rates for SPH particles (dots) and contact shear rates (continuous lines) at 40% volume fraction in a shear thinning (red), Newtonian (black) and shear thickening (blue) fluid. **(b)** SPH particles (dots) and contact shear rate probability densities (continuous lines) for a shear thinning suspension at 20%(red), 40% (green) and 50% (blue) volume fraction. *Inset :* Log-linear representation of the contact shear rates probability density.

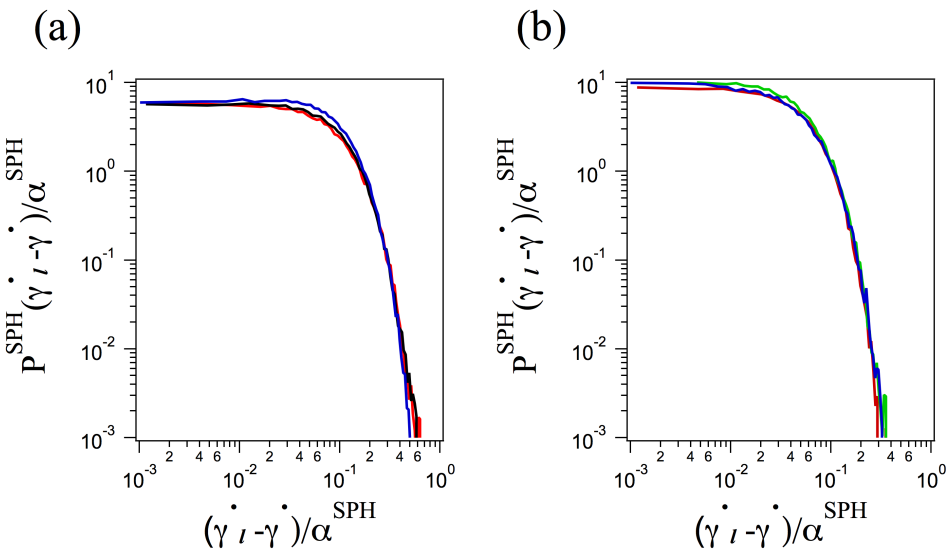

FIG. 8. **(a)** Rescaled SPH particles shear rate probability densities at 40% volume fraction in a shear thinning (red), Newtonian (black) and shear thickening (blue) fluid, under $\dot{\gamma} = 30$ s^{-1}. **(b)** Rescaled SPH particles shear rate probability densities for a shear thinning suspension at 20%(red), 40% (green) and 50% (blue) volume fraction, under $\dot{\gamma} = 30$ s^{-1}. The shift factors α^{SPH} are computed with Eq. 34.

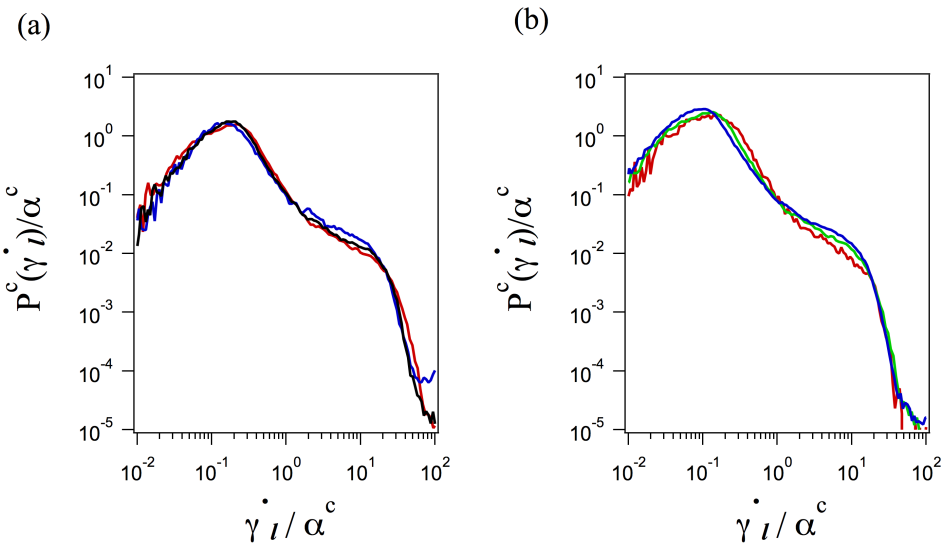

FIG. 9. Rescaled contact shear rate probability densities for shear thinning (red), Newtonian (black) and shear thickening (blue) suspensions at 40% volume fraction under $\dot{\gamma} = 30$ s^{-1}. **(b)** Rescaled contact shear rate probability densities for shear thinning suspension at 20 (red), 40 (green) and 50 (blue) % volume fraction under $\dot{\gamma} = 2\dot{\gamma}^*$. The shift factors α^c are computed with Eq. 33.

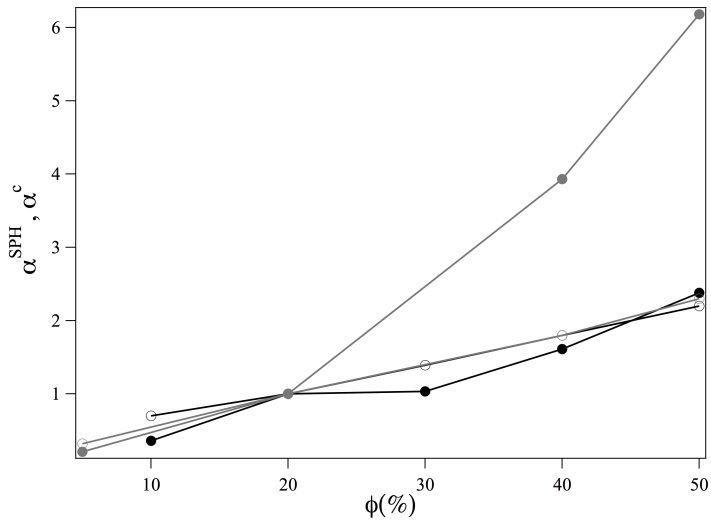

FIG. 10. Evolution of the scaling factors, $\alpha^c(\phi, \phi_0 = 20\%)$ (full disks) and $\alpha^{SPH}(\phi, \phi_0 = 20\%)$ (empty circles) with the volume fraction, for the shear thinning (dark symbols) and shear thickening (grey symbols) fluids, under $\dot{\gamma} = 2\dot{\gamma}^*$. The master curve for rescaling is the 20 % volume fraction curve.

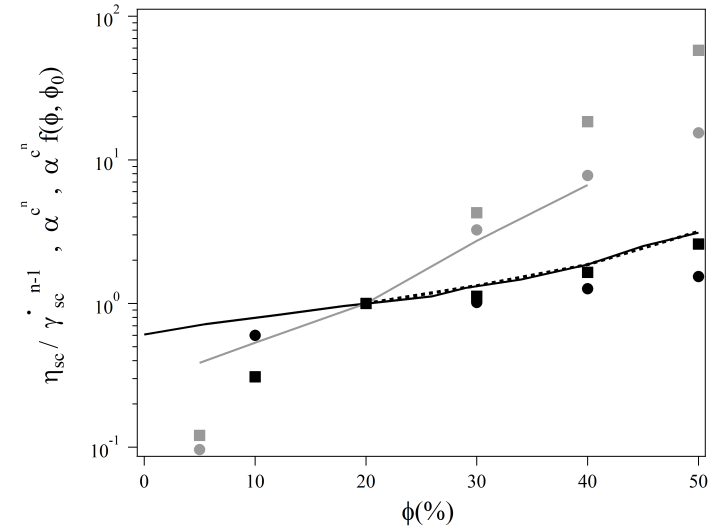

FIG. 11. Ratio of the macroscopic scaling parameters, using the 20 % volume fraction flow curve as the master curve, $\eta_{sc}/\dot{\gamma}_{sc}^{n-1}$ obtained *via* experiments (continuous lines) and *via* SPH-simulation (dashed lines), and microscopic scaling factor α^{c^n} (full disks) and $\alpha^{c^n} f(\phi, \phi_0)$ (full squares) as a function of the volume fraction. Results are given for the shear thinning (black) and the shear thickening (grey) suspensions, under $\dot{\gamma} = 2\dot{\gamma}^*$.